

The influence of magnetic fields in Cloud-Cloud Collisions.

Theotokis Georgatos,[★] Anthony P. Whitworth,

School of Physics and Astronomy, Cardiff University, Queens Buildings, The Parade, Cardiff CF24 3AA, Wales, UK

Accepted XXX. Received YYY; in original form ZZZ

ABSTRACT

Cloud–cloud collisions are expected to trigger star formation by compressing gas into dense, gravitationally unstable regions. However, the role of magnetic fields in this process is unclear. We use SPH to model head-on collisions between two uniform density clouds, each with mass $500 M_{\odot}$, initial radius 2 pc, and embedded in a uniform magnetic field parallel to the collision velocity. As in the non-magnetic case, the resulting shock-compressed layer fragments into a network of filaments. If the collision is sufficiently slow, the filaments are dragged into radial orientations by non-homologous gravitational contraction, resulting in a *Hub Filament* morphology, which spawns a centrally concentrated monolithic cluster with a broad mass function shaped by competitive accretion and dynamical ejections. If the collision is faster, a *Spiders Web* of intersecting filaments forms, and star-systems condense out in small subclusters, often at the filament intersections; due to their smaller mass reservoirs, and the lower probability of dynamical ejection, the mass function of star-systems formed in these subclusters is narrower. Magnetic fields affect this dichotomy quantitatively by delaying collapse and fragmentation. As a result, the velocity threshold separating *Hub Filament* and *Spiders Web* morphologies is shifted upward in magnetised runs, thereby enlarging the parameter space in which *Hub Filament* morphologies form, and enhancing the likelihood of producing centrally concentrated clusters. Consequently magnetic fields regulate both the morphology and timing of star formation in cloud–cloud collisions: they broaden filaments, delay the onset of star formation, and promote the formation of *Hub Filament* morphologies, monolithic clusters and high-mass star-systems.

Key words: stars: formation – stars: protostars – stars: statistics – ISM: clouds – shock waves – (magnetohydrodynamics) MHD

1 INTRODUCTION

Cloud–cloud collisions (CCCs) are a compelling mechanism for triggering star formation on galactic scales (Inoue & Fukui 2013; Wu et al. 2017; Fukui et al. 2021a; Horie et al. 2024; Maity et al. 2024; Weis et al. 2024). When two clouds collide at supersonic speed, they produce a dense, shock-compressed layer, which rapidly accumulates mass and may become gravitationally unstable. Unlike isolated clouds, a significant role is played by the ram pressure of continuing gas inflow, making the shock-compressed layer a conducive environment for the formation of prestellar cores, especially massive cores (e.g. Hsu et al. 2023). It is therefore important to explore what effect a magnetic field has on this scenario.

The frequency of CCCs—and consequently their cumulative impact on star formation—is difficult to quantify (see Haworth et al. 2015; Gong et al. 2019). On the basis of hydrodynamic simulations, Dobbs et al. (2015) conclude that clouds experience very few collisions during their lifetime, and therefore cloud evolution is little affected by collisions. On the other hand, Balfour et al. (2016) estimate that relatively low-mass, low-velocity CCCs are frequent in the Galaxy, and could play a dominant role in regulating the overall rate of star formation.

Observationally, identifying cases of star formation triggered by CCCs remains challenging, thereby limiting our ability to assess the

influence of CCCs on star formation (Haworth et al. 2015). Certain diagnostic features (Fukui et al. 2018a,b; Maity et al. 2024), for example a "bridge" feature connecting two colliding clouds in position–velocity space, have been proposed as indicators. However, these signatures are often difficult to detect, due to their strong dependence on viewing angle and chemistry (e.g. Priestley & Whitworth 2021).

There have been several studies of star formation triggered by CCCs (for example Whitworth et al. 1994a,b; Kitsionas & Whitworth 2007; Whitworth 2016; Dinnbier et al. 2017; Whitworth et al. 2018; Priestley & Whitworth 2021; Whitworth et al. 2022). Balfour et al. (2015) use pure hydrodynamic simulations to demonstrate that a low-velocity collision produces a shock compressed layer, which then fragments into a network of filaments. They show that the shock-compressed layer fragments into two distinct morphologies depending on whether the initial collision velocity exceeds a velocity threshold Δu_{thresh} .

For high-speed collisions (relative velocity greater than $\Delta u_{\text{thresh}} \sim 3.0 \text{ km s}^{-1}$) the layer builds up sufficiently fast that fragmentation occurs before the layer has had time to contract laterally (i.e. orthogonal to the collision axis). This results in a network of intersecting filaments resembling a *Spiders Web*. Low-mass cores form out of the filaments, often at their intersections, and a small subcluster condenses out of each core. The mass reservoir in each core is low, so it is hard for very massive stars to form there. The number of stars is small, so there is little opportunity to dynamically eject low-mass stars, thereby terminating their growth. As a result the stellar mass function is relatively narrow. Only when star formation is largely

[★] E-mail: GeorgatosT@Cardiff.AC.UK

complete do these subclusters fall together and relax to form a larger cluster.

In contrast, for collisions with relative velocities below Δu_{thesh} , the layer builds up more slowly and at the same time contracts laterally and non-homologously (i.e. faster towards the centre). This non-homologous contraction drags the forming filaments into radial orientations so that by the time they start to fragment they are already feeding their material towards a monolithic central massive core, resulting in an *Hub Filament* morphology. In the central massive core, stars grow by competitive accretion. Consequently a few stars attain very high masses, and others are ejected dynamically thereby cutting off accretion and limiting them to very low masses. The result is a centrally concentrated monolithic cluster with a broad mass function.

A critical issue is then whether magnetic fields influence the separatrix between circumstances that produce *Spiders Web* morphologies and those that produce *Hub Filament* morphologies. Since the underlying filamentary structure governs how material is delivered to protostar-systems, any such magnetic regulation is expected to have a direct impact on the morphology of star-system formation and the resulting mass function.

MHD simulations of high velocity CCCs by [Inoue & Fukui \(2013\)](#) and [Fukui et al. \(2021b\)](#) demonstrate that collisions between clouds of $\sim 10^4 M_{\odot}$ with relative velocities of 10 km s^{-1} can produce massive fragments of order $50 M_{\odot}$. This suggests that massive stars may form in high-velocity collision environments.

Simulations of cloud–cloud collisions between unequal-mass clouds by [Sakre et al. \(2021\)](#), and spanning a range of magnetic field strengths and collision velocities up to 10 km s^{-1} , suggest that stronger magnetic fields can facilitate the formation of high-mass cores. They attribute this conclusion to the suppression of low-mass core growth and the stabilisation of the shock-compressed layer.

In contrast, on the basis of simulations involving higher collision velocities in the range 20 to 40 km s^{-1} , [Sakre et al. \(2023\)](#) conclude that magnetic fields may inhibit massive core formation by limiting post-collision gas accretion. Enhanced magnetic pressure drives rapid expansion of the shock-compressed region, leading to the disruption of gravitationally unbound cores. This implies that collision velocity is a key factor in determining whether magnetic fields promote or suppress massive core growth.

These MHD studies of CCCs have demonstrated that magnetic fields alter fragmentation and core formation in colliding clouds (e.g. [Inoue & Fukui 2013](#); [Fukui et al. 2021b](#); [Sakre et al. 2021, 2022, 2023](#)), but we are unaware of any studies that have systematically explored how varying both the initial field strength, and the collision velocity, affects filament widths, stellar mass functions, and measures of stellar clustering.

In this study, we model CCCs using initial conditions similar to those of [Balfour et al. \(2015\)](#), with the addition of a magnetic field aligned parallel to the collision axis. Our aim is to identify, and where possible quantify, the effects of a magnetic field on the resulting star-system formation, using very simplistic initial conditions and constitutive physics, rather than to reproduce accurately all the features of observed systems. Therefore we refer to our models as numerical experiments, rather than simulations.

The remainder of the paper is organised as follows. Section 2 describes the initial conditions for the numerical experiments. Section 3 sketches the main physical processes at work in the experiments. Section 4 presents the results. In Section 5, we discuss the implications of the results, and in Section 6 we summarise our main conclusions.

Table 1. Parameters describing the initial conditions.

Initial cloud radius	$R_o = 2 \text{ pc}$
Cloud mass	$M_o = 500 M_{\odot}$
Initial cloud density	$\rho_o \approx 10^{-21} \text{ g cm}^{-3}$
Isothermal sound speed in cloud	$a_o = 0.187 \text{ km s}^{-1}$
Background density	$\rho_{\text{back}} = 10^{-23} \text{ g cm}^{-3}$
Isothermal sound speed in background	$a_{\text{back}} \approx 1.87 \text{ km s}^{-1}$
Relative collision velocities	$\Delta u_o = 2u_o = 2.4, 2.8, 3.2, 3.6, 4.0, 4.4 \text{ km s}^{-1}$
Mach Number of collision	$\mathcal{M}_o = u_o/a_o = 6.4, 7.5, 8.5, 9.6, 10.7, 11.7$
Magnetic fields	$B_o = 0, 1, 2, 3.3, 5 \mu\text{G}$
Sink creation density threshold	$\rho_{\text{sink}} = 10^{-16} \text{ g cm}^{-3}$
Sink radius	$R_{\text{sink}} = 600 \text{ au} = 0.003 \text{ pc}$
Size of the computational domain	$L_o = 8 \text{ pc}$
Number of SPH particles	$N_{\text{SPH}} \approx 10^6$

Table 2. Glossary

<i>Layer Accumulation</i>	accumulation of a shock-compressed layer orthogonal to the collision axis
<i>Lateral Contraction</i>	reduction of the extent of a shock-compressed layer orthogonal to the collision axis
<i>Layer Fragmentation</i>	break-up of a shock-compressed layer driven by self-gravity
<i>Spiders Web</i>	an isotropic network of randomly oriented filaments (e.g. bottom left panel of Fig. 2)
<i>Hub Filament</i>	an isotropic array or radially oriented filaments (e.g. top right panel of Fig. 2)

2 NUMERICAL METHODS AND INITIAL CONDITIONS

We model CCCs using the publicly available Smoothed-Particle Magneto-Hydrodynamics (SPH) code **PHANTOM** ([Price et al. 2018](#)), with initial conditions analogous to those in [Balfour et al. \(2015\)](#). The default [Morris & Monaghan \(1997\)](#) viscosity prescription is adopted.

Each cloud has mass $M_o = 500 M_{\odot}$ and radius $R_o = 2 \text{ pc}$, corresponding to a uniform density $\rho_o = 10^{-21} \text{ g cm}^{-3}$. The cloud gas has isothermal sound speed $a_o = 0.187 \text{ km s}^{-1}$, corresponding to molecular gas with solar elemental abundances and gas-kinetic temperature $T_o = 10 \text{ K}$.

The cloud centres are initially located at

$$[x, y, z] = [\pm 2.0, 0, 0] \text{ pc}, \quad (2.1)$$

with bulk velocities

$$[u_x, u_y, u_z] = [\mp u_o, 0, 0]. \quad (2.2)$$

Consequently the clouds immediately collide head-on, with relative velocity $\Delta u_o = 2u_o$.

The colliding clouds are envisaged as part of a larger cloud complex with mass in the range $\sim 2,000$ to $\sim 20,000 M_{\odot}$. Thus, adopting Larson's scaling relations for the velocity dispersion within a cloud complex ([Larson 1981](#), $\sigma_v \sim 0.42 \text{ km s}^{-1} (M/M_{\odot})^{0.20}$), we assign cloud velocities $u_o \sim 1.0, 1.2, 1.4, 1.6, 1.8, 2.0, 2.2$ and 2.4 km s^{-1} . The relative velocities of the clouds are therefore $\Delta u_o \sim 2.0, 2.4, 2.8, 3.2, 3.6, 4.0, 4.4$ and 4.8 km s^{-1} .

The clouds are embedded in a hot, low-density background with density $\rho_{\text{back}} = \rho_o/100$ and isothermal sound speed $a_{\text{back}} = 10a_o$. This ensures approximate pressure balance at the cloud boundaries.

The initial magnetic field strength, B_o , is set to a fraction, β_o , of the critical value for the magnetic field to balance the self-gravity of

the cloud (Chandrasekhar & Fermi 1953),

$$B_{\text{crit}} = 2\pi G^{1/2} \rho_0 R_0, \quad (2.3)$$

$$B_0 = \beta_0 B_{\text{crit}}. \quad (2.4)$$

We adopt five magnetic field strengths corresponding to $\beta_0 = 0, 1/10, 1/5, 1/3$, and $1/2$. This yields field strengths of $B_0 \sim 0, 1, 2, 3.3$ and $5 \mu\text{G}$. We have checked that – for the collision velocities considered here – fragmentation of the shock-compressed layer into filaments is entirely suppressed with $\beta_0 = 1$ ($B_0 = 10 \mu\text{G}$). The uniform initial magnetic field is parallel to the collision axis x , i.e. $\mathbf{B} = [B_0, 0, 0]$. This uniform magnetic field threads the entire computational domain.

The computational domain is a cube with side $L_0 = 8 \text{ pc}$ and we adopt periodic boundary conditions. The initial distribution of SPH particles is generated by relaxing a periodic box into a glass-like distribution and then cutting out a sphere with radius $R_0 = 2 \text{ pc}$ to represent a cloud. The sphere is then rotated through random Euler angles. Different random rotations are used for the two clouds. To generate the background a similar glass distribution is generated, with 100 times lower particle density, and two spherical holes are cut to accommodate the clouds. The SPH particles representing the background are not rotated. The clouds are modelled with $N_{\text{SPH}} \simeq 10^6$ particles and each particle has approximately 57 neighbours, yielding a minimum resolved mass of $\sim 0.1 \text{ M}_\odot$.

Sink particles are introduced at a density threshold $\rho_{\text{sink}} = 10^{-16} \text{ g cm}^{-3}$, using the Bate et al. (1995) prescription. Sink merging is turned off, and the sink radius is set to $R_{\text{sink}} = 600 \text{ au}$, with only gas within 180 au being unconditionally accreted.

We shall refer to sinks as star-systems, because our numerical experiments are unable to resolve wither below the Hydrogen Burning Limit, or any but the widest binary orbits. Thus ‘star-systems’ could be single stars, binaries and higher-order multiples, or even just small subclusters that have not had time to relax dynamically.

The parameters of the initial conditions and constitutive physics are summarised in Table 1. For each combination of B_0 and Δu_0 we run three realisations, each with different initial distributions of SPH particles (i.e. different random rotation angles).

Since the model does not include stellar feedback, we terminate experiments once 10% of the mass has been converted into star-systems, since by then feedback processes are likely to be important. We refer to this time as $t_{10\%}$, and most of the statistics that we present are collated at $t_{10\%}$, combining the three realisations of each $(B_0, \Delta u_0)$ combination.

In the sequel, the x axis – which is parallel or anti-parallel to both the initial cloud velocities and the initial magnetic field – is described as the collision axis; vector components parallel to the x axis are described as ‘axial’ and denoted with subscript ‘ x ’, e.g. axial magnetic field B_x . Conversely, vector components orthogonal to the x axis are termed ‘lateral’, and denoted with a subscript ‘ yz ’, e.g. lateral magnetic field $B_{yz} \equiv (B_y^2 + B_z^2)^{1/2}$.

3 GLOBAL PHYSICAL PROCESSES

As in the non-magnetic case (Balfour et al. 2015), the colliding clouds produce a shock-compressed layer, which may eventually become sufficiently massive to fragment into filaments and cores, and spawn star-systems. In this section we isolate and define the critical global physical processes which contribute to the evolution of colliding clouds.

3.1 No magnetic field, fast collision

The simplest setup involves no magnetic field, $B_0 = 0$, and a relatively high collision speed, $\Delta u_0 \gtrsim 3.2 \text{ km s}^{-1}$ ($\mathcal{M}_0 > 20$). There are then just two basic processes, *Layer Accumulation* and *Layer Fragmentation*, and they are approximately sequential.

Layer Accumulation describes the assembly of the layer by the colliding clouds. The surface-density builds up to $\Sigma_{\text{MAX}} \sim 4R_0 \rho_0$ at a rate $\dot{\Sigma} \sim \rho_0 \Delta u_0$, and therefore on a timescale $t_{\text{ACC}} \sim 4R_0 / \Delta u_0$.

Layer Fragmentation describes the break-up of this layer due to self-gravity, and requires $\Sigma_{\text{MAX}} \gtrsim a_0^2 / 2\pi G R_0$, or equivalently $\mathcal{M}_0 / R_0 \gtrsim a_0^2 / 4G$. Fragmentation proceeds through the formation of a network of intersecting filaments, which we term a *Spiders Web*. A multitude of small cores then forms, often at the intersections of the filaments, and then star-systems condense out of the cores.

The individual cores have a small mass reservoir, and consequently the stars formed in them have a relatively small mass-range. There is insufficient mass to form very high-mass stars. There are also too few stars for many very low-mass stars to be formed by having their ongoing accretion abruptly terminated by dynamical ejection from the core.

The star-systems formed from the different individual small cores eventually fall together and relax to form a single star cluster, but by then the masses of the stars have essentially been determined, and further growth by accretion is a small perturbation to the overall mass spectrum.

3.2 No magnetic field, slow collision

If there is still no magnetic field, $B_0 = 0$, but the collision is relatively slow, $\Delta u_0 \lesssim 2.8 \text{ km s}^{-1}$ ($\mathcal{M}_0 < 10$), a third process comes into the reckoning, namely *Lateral Contraction*.

Lateral Contraction describes the convergence of material towards the x axis, driven by the global self-gravity of the two clouds, and it occurs on a timescale $t_{\text{LAT}} \simeq \{3G\rho_0\}^{-1/2}$. This has two important effects.

Firstly, during *Layer Accumulation*, *Lateral Contraction* causes the approximately circular patch where the clouds collide to shrink, and therefore build-up of the critical surface-density is accelerated.

Secondly, during *Layer Fragmentation*, *Lateral Contraction* is non-homologous: the central parts of the layer converge on the x axis faster than the outer parts. This drags the forming filaments into radial orientations, so that instead of feeding material into a multitude of small isolated cores, the filaments channel material into a central monolithic hub. Here, competitive accretion promotes the formation of very high-mass stars. In addition, very low-mass stars are created more frequently by having their on-going accretion abruptly terminated by dynamical ejection.

Some of the material arriving in the central core has already been converted into stars, but much of it arrives in the form of gas, and is therefore available to be accreted by existing stars, as well as forming additional stars. The stars form and grow in a single proto-cluster, and the resulting star cluster has a broad mass spectrum.

3.3 The effects of a sub-critical magnetic field

At the densities ($\lesssim \rho_{\text{sink}} = 10^{-16} \text{ g cm}^{-3}$), and on the timescales ($\lesssim 1 \text{ Myr}$) considered here, it is reasonable to adopt ideal magnetohydrodynamics. The gas is treated as a single fluid, which can move freely along the local field line but can only move orthogonal to the local field line if it drags the field line with it. The introduction of a magnetic field therefore has the following main effects.

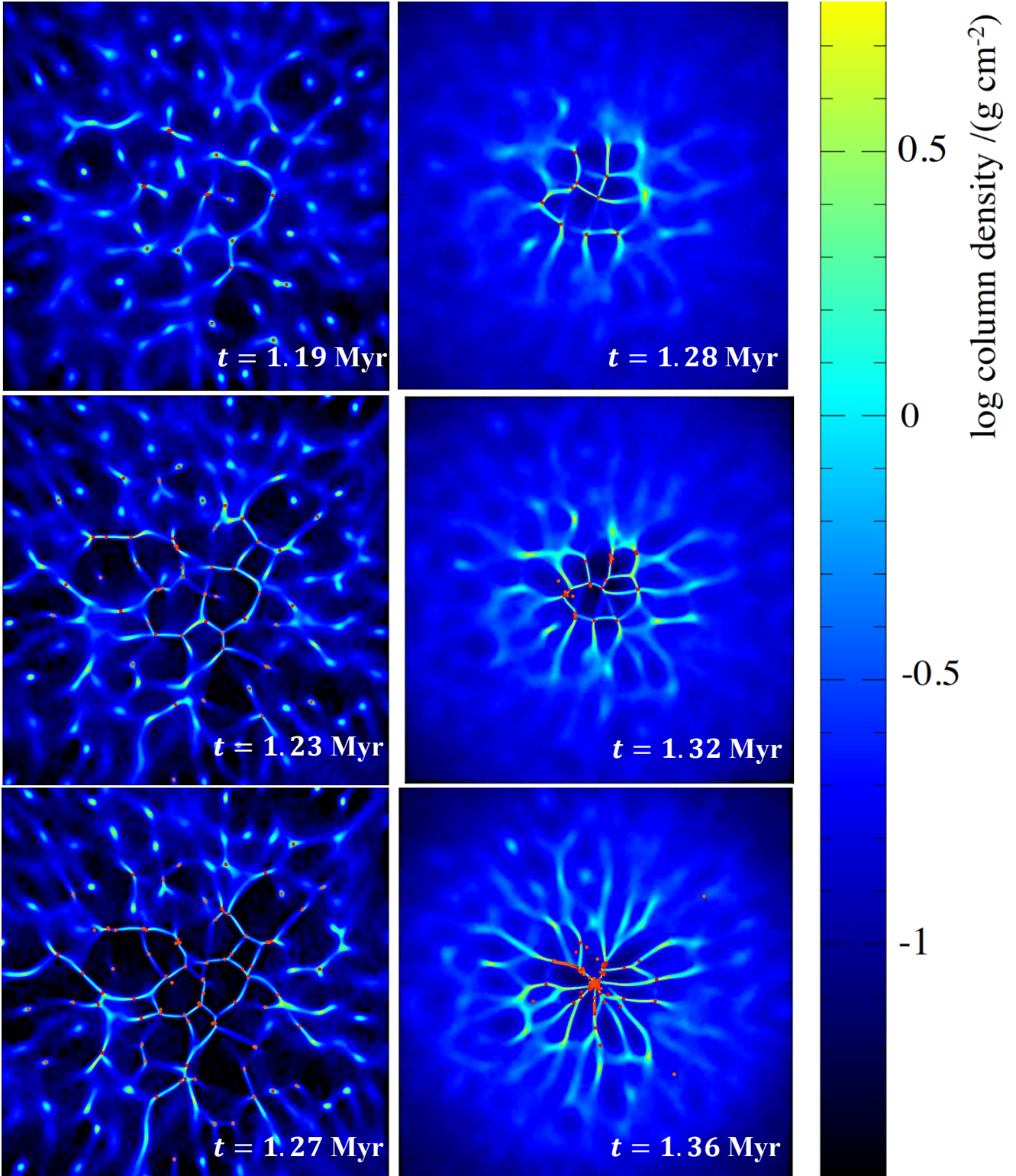


Figure 1. False-colour surface-density maps looking along the x axis and therefore face-on to the layer, showing the evolution of the filamentary network for collisions at $\Delta u_0 = 3.6 \text{ km s}^{-1}$. *Left panels:* no magnetic field, $B_0 = 0$. *Right Panels:* strong magnetic field, $B_0 = 5 \mu\text{G}$. Each panel has dimensions $1\text{pc} \times 1\text{pc}$. Times from the start of the collision are shown in the bottom right corner of each panel; each sequence spans 0.08 Myr and ends at $t_{10\%}$. The colour scale is logarithmic. For gas with solar composition, 1 g cm^{-2} corresponds to $\sim 2.1 \times 10^{23} \text{ H}_2 \text{ cm}^{-2}$. Red dots mark the locations of star-systems. Maps have been generated using SPLASH (Price 2007).

Firstly, there is an additional force resisting self-gravity in directions orthogonal to the field. In effect the gravitational constant is reduced by a factor of order $(1 - \beta_0^2)$ in these directions.

Secondly, the flows that lead to the formation of filaments, then cores, and finally star-systems, tend to be aligned with the local field.

As a result, during *Layer Accumulation*, *Lateral Contraction* increases the strength of the axial magnetic field, B_x , by squeezing the field lines together, i.e. by reducing the size of the approximately circular patch where the field lines intercept the layer. Additionally the axial magnetic field increases the minimum surface-density required for fragmentation to occur, so that the *Layer Accumulation* phase takes longer.

Only during the subsequent *Layer Fragmentation* phase do the motions that collect the material of the layer into filaments create a lateral magnetic-field component, B_{yz} , i.e. parallel to the midplane of the layer. In the end all components of the magnetic field are increased by the convergent motions delivering mass onto and along filaments, and into cores. The magnetic field components at the highest densities tends towards equipartition ($B_{yz} \sim 2^{1/2} B_x$; see Section 4.5).

4 RESULTS

4.1 The Filamentary Network

Figure 1 shows a time-sequence of three surface-density maps (time increasing from top to bottom), for two different setups: the setup for the three left panels has no magnetic field; and the setup for the three right panels has a magnetic field. These maps illustrate the time evolution of the filamentary network, from the viewpoint of an observer looking along the collision axis and therefore face-on to the shock-compressed layer. The collision velocity is the same for the two setups, so the rate at which the shock compressed layer builds up, $\dot{\Sigma} \sim 2\rho_0 u_0$, is also more-or-less the same. The differences are therefore almost entirely attributable to the fact that in one case there is no magnetic field and in the other there is.

The three maps in the lefthand column of Figure 1 are from an experiment with no magnetic field ($B_0 = 0$) and collision velocity $\Delta u_0 = 3.6 \text{ km s}^{-1}$. With no magnetic field the layer fragments quickly – i.e. before there has been significant *Lateral Contraction* – and forms a *Spiders Web* of filaments. Small cores form, more-or-less independently of one another, and often at the intersections of the filaments. Small star-systems then condense out of these cores. The limited mass reservoir in an individual core is reflected in the relatively narrow mass function of the star-systems formed. There is not enough mass to form very high-mass stars, and there are few stars and therefore few violent dynamical interactions that might eject a stellar embryo, thereby cutting off accretion and creating a very low-mass star.

The three maps in the righthand column of Figure 1 are from an experiment with a strong magnetic field, $B_0 = 5 \mu\text{G}$, but the same collision velocity, $\Delta u_0 = 3.6 \text{ km s}^{-1}$. In this case, due to the additional magnetic pressure, the layer has to build up to a larger surface-density before it starts fragmenting, and it also fragments into filaments and cores more slowly (than in the non-magnetic case). There is therefore more time for *Lateral Contraction*, and since *Lateral Contraction* is non-homologous – in the sense that the central parts of the layer contract on a shorter timescale than the outer parts – the filaments are dragged into radial orientations. Consequently material is fed into a central monolithic core, where very high-mass star-systems can grow by competitive accretion; and also there are frequent dynamical interactions ejecting stellar embryos, terminating their growth and producing very low-mass star-systems.

Star-systems usually start to condense out before their material arrives in the monolithic central core, but growth by accretion and dynamical ejection become important once they arrive in the central core.

We note that in the non-magnetic case filaments become increasingly narrow as the evolution progresses. This narrowing is predicted for an isothermal filament (strictly speaking, an isolated semi-infinite isothermal filament) by [Inutsuka & Miyama \(1992\)](#).

Figure 2 shows four surface-density maps, all at $t_{10\%}$, but corresponding to different combinations of field strength B_0 and collision velocity Δu_0 . The maps in the left column represent setups with no magnetic field ($B_0 = 0$), and those in the right column represent setups with a strong magnetic field ($B_0 = 5 \mu\text{G}$). The maps on the top row are for relatively low collision velocities ($\Delta u_0 = 2.4 \text{ km s}^{-1}$), and those on the bottom row are for relatively high collision velocities ($\Delta u_0 = 3.6 \text{ km s}^{-1}$).

These maps are intended to reinforce the dichotomy between setups that evolve through a *Spiders Web* morphology (bottom-left panel) and produce star-systems that are initially widely distributed and relatively isolated from one another; and setups that evolve through an *Hub Filament* morphology (the other three panels) and produce star-systems in a monolithic star cluster, and therefore stars with a relatively broad mass function. In Section 4.8 we discuss the consequences of this dichotomy for the spatial distribution of young stars-systems.

4.2 Tracing Filaments

To trace the filamentary network and extract the properties of filaments, we generate high-resolution surface-density maps like those illustrated on Figures 1 and 2. Next we convolve these maps with a Gaussian kernel having a full width at half maximum, $\text{FWHM} \sim 0.01 \text{ pc}$, corresponding to the Herschel SPIRE 250 μm beam width at a distance of $\sim 140 \text{ pc}$ (this ensures that the filament properties can be compared with observed filaments like the Taurus B211/3 filament, e.g. [Palmeirim et al. 2013; Howard et al. 2019](#)). Finally we apply the FILFINDER Python module ([Koch & Rosolowsky 2015](#)): pixels exceeding the local median intensity define the filament spine and allow us to construct filament masks; radial profiles are extracted out to 0.2 pc from the spine; each profile is then background-subtracted and fitted with a Gaussian profile to obtain the FWHM.

4.3 Filament FWHMs

Figure 3 shows the normalised distributions of filament FWHMs for three different values of the initial magnetic field strength, $B_0 = 0, 3.3$ and $5.0 \mu\text{G}$. The mean FWHM increases monotonically with increasing B_0 . This is (a) because the *lateral* field strength, B_{yz} , in the shock compressed layer increases with increasing B_0 (see Section 4.5); and (b) because inside a filament the field tends to be aligned with the spine of the filament (see Section 4.4), thereby giving the filament additional support orthogonal to its spine.

The distribution of filament FWHMs for a given B_0 (i.e. an individual panel on Figure 3) is generated by combining results from three independent realisations for each different collision velocity. In reality, the filament width also depends – albeit weakly – on the collision velocity, in the sense that the filaments tend to be slightly broader for lower collisions velocity, because the magnetic field is then amplified more by *Lateral Contraction* (see Section 4.5). However, the dependence of filament width on B_0 is much stronger than the dependence on Δu_0 .

Along with several studies that have explored whether the appearance of a universal filament FWHM may arise from methodological

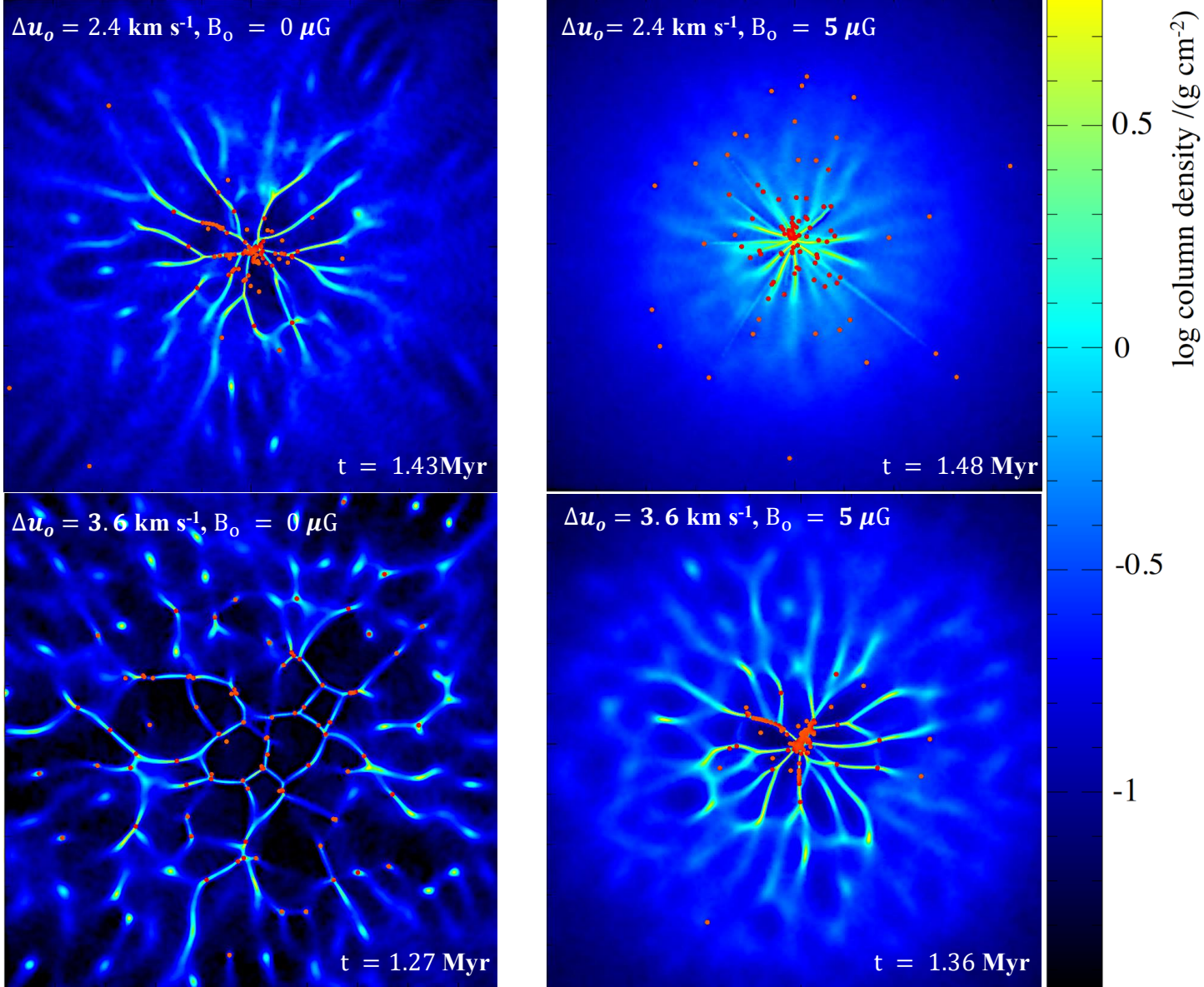


Figure 2. False-colour surface-density maps at $t = t_{10\%}$, looking along the x axis and therefore face-on to the layer. *Left panels*: no magnetic field, $B_0 = 0$. *Right Panels*: strong magnetic field, $B_0 = 5 \mu\text{G}$. *Top Panels*: lower collision velocity $\Delta u_0 = 2.4 \text{ km s}^{-1}$. *Bottom Panels*: higher collision velocity $\Delta u_0 = 3.6 \text{ km s}^{-1}$. The initial magnetic field, B_0 , and the collision velocity, Δu_0 , are given in the top lefthand corner of each frame, and the value of $t_{10\%}$ in the bottom righthand corner. The colour scale is logarithmic. For gas with solar composition, 1 g cm^{-2} corresponds to $\sim 2.1 \times 10^{23} \text{ H}_2 \text{ cm}^{-2}$. Red dots mark the locations of star-systems. Maps have been generated using SPLASH (Price 2007).

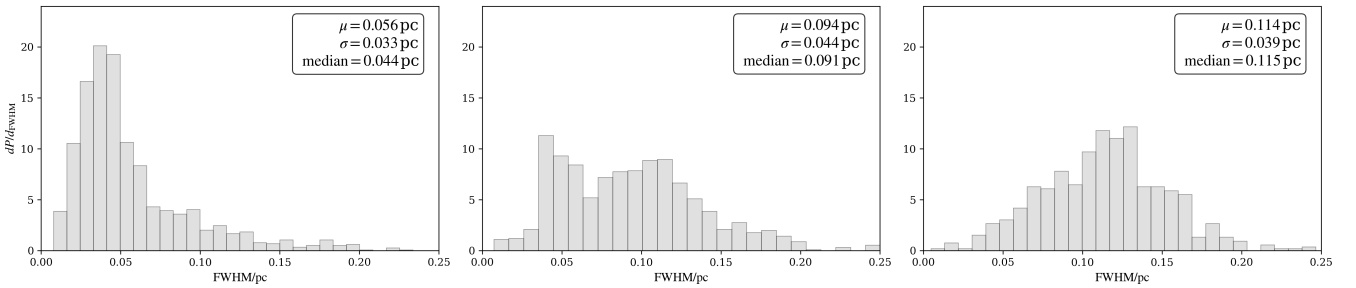


Figure 3. The normalised distribution of filament widths (FWHM) for different magnetic field strengths: *Left Panel*, no field, $B_0 = 0$; *Middle Panel*, intermediate field, $B_0 = 3.3 \mu\text{G}$; *Right Panel*, strong field $B_0 = 5 \mu\text{G}$. The mean, standard deviation and median of the FWHM, are shown in the top righthand corner of each panel. Each panel represents the results obtained from all the experiments obtained with that B_0 value, i.e. three realisations for each value of Δu_0 .

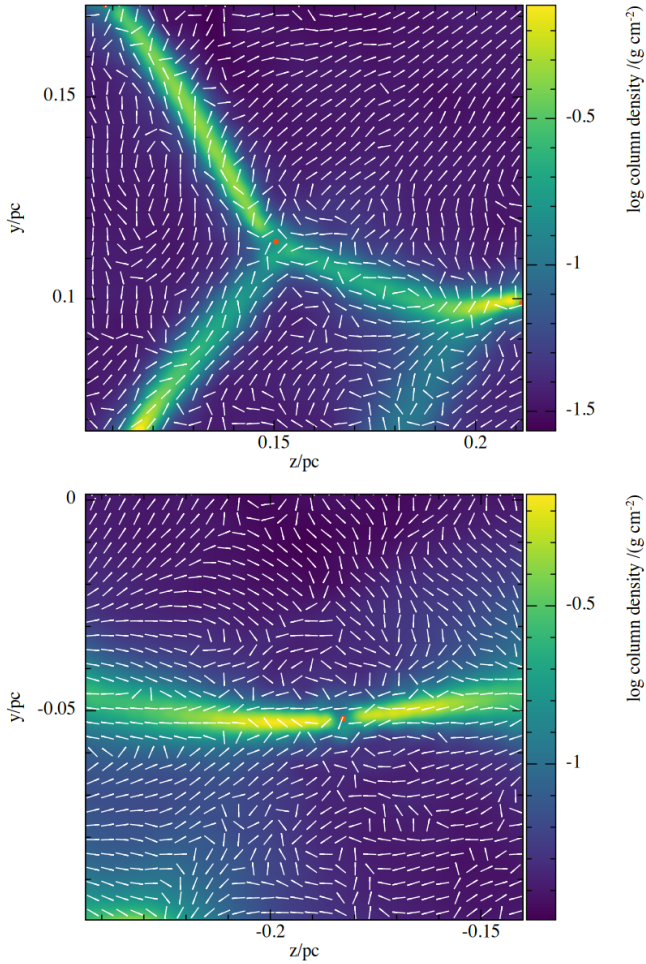


Figure 4. Zoom-in false-colour surface-density maps showing the filamentary structures and magnetic field lines in the vicinity of representative star-systems: *Top Panel*, a star-system formed at the intersection of three filaments; *Bottom Panel*, a star-system formed in the middle of a filament. The colour-scale representing surface-density is logarithmic, and the white lines indicate the direction of the lateral magnetic field, B_{yz} . Red dots mark sink locations.

biases or environmental dependence (Smith et al. 2016; Panopoulou et al. 2017, 2022; Hacar et al. 2018), our results support a nuanced view. The FWHM of ~ 0.1 pc frequently reported on the basis of Herschel observations of nearby clouds (Arzoumanian et al. 2011; André et al. 2016) is unlikely to be universal, and a range of values seems more likely. In the colliding cloud setup explored here, this range reflects both the field-strength and the collision velocity.

4.4 Alignment between Filaments and the Magnetic Field

As the shock-compressed layer contracts laterally and fragments, the gas flowing into the layer is deflected, creating a lateral magnetic field component, B_{yz} , which is then stretched and compressed. A stronger initial field, B_0 , generally results in a stronger lateral field, B_{yz} , in the shock-compressed layer (see Section 4.5).

Figure 4 shows the structure of the magnetic field in the vicinities of two cores, one that has formed in the middle of a filament and another that has formed at the intersection of three filaments. In most places the field in a filament is close to parallel with the filament spine. Under this circumstance, flow along the filament is not impeded by the

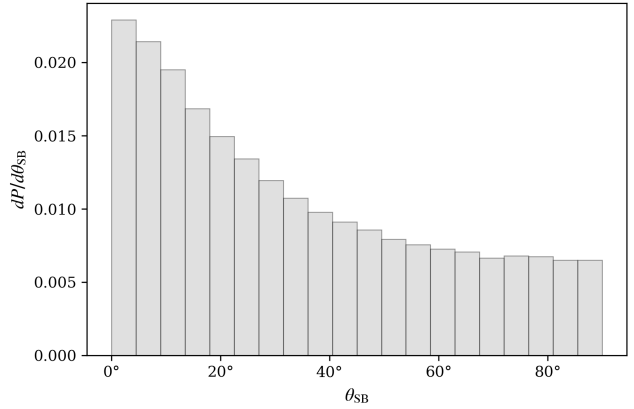


Figure 5. The normalised distribution of angles, θ_{SB} , between the filament spines and the local magnetic field at $t_{10\%}$. This plot derives from all the experiments (three realisations for each combination of B_0 and Δu_0).

Lorentz force. However, in some places, where material has accreted along a field-line and onto a filament (i.e. the field near the filament has a large component orthogonal to the spine of the filament), the flow along the filament has had to drag the field with it, leading to a field reversal across the filament spine.

Figure 5 shows the distribution of the angles, θ_{SB} , between filament spines and the local magnetic field.¹ There is a clear preference for alignment between the spine and the field. The extra support from the aligned field then results in broader filaments, as discussed in Section 4.3 and shown on Figure 3.

4.5 The magnetic field strength

Figure 6 shows how the magnetic field strength depends on the density, at the end of the experiment ($t_{10\%}$), for collision velocities $\Delta u_0 = 2.4, 3.6$ and 4.4 km s^{-1} . The plotted quantity is strictly speaking an average magnetic field, $\bar{B}(\rho)$, but the standard deviation of the magnetic field at a given density is seldom large, typically $\sigma_{\log_{10}(B)} \lesssim 0.2$. Results are not presented for densities $\rho < \rho_0 = 10^{-21} \text{ g cm}^{-3}$, since the gas that forms the layer (and subsequently filaments and star-systems) never attains such low densities. Conversely, we do not show results for densities $\rho > \rho_{\text{sink}} = 10^{-16} \text{ g cm}^{-3}$, since there is very little of it, almost all of it has been assimilated by star-systems. There are several things to note from this plot.

Firstly, amplification of the field is quite modest, particularly for rapid collisions. Once the field has been deflected to create a lateral component and filaments have formed aligned with this lateral component, the motions collecting material into cores are predominantly along the field, and therefore do not greatly increase the field strength.

For rapid collisions, the *Layer Accumulation* and *Layer Fragmentation* phases are relatively quick, and there is little *Lateral Contraction* and hence little field compression. For example, with $B_0 = 5 \mu\text{G}$ and $\Delta u_0 = 4.0 \text{ km s}^{-1}$, the field is only amplified by a factor ~ 10 over the 10^5 -fold density increase between $10^{-21} \text{ g cm}^{-3}$ and $10^{-16} \text{ g cm}^{-3}$.

¹ In reality, projection onto the $x = 0$ plane does not significantly change either the direction of the spine of a filament, or the direction of the magnetic field in a filament. Random relative orientation is therefore given by the 2D form, $dP/d\theta_{SB} \simeq 1/90^\circ$, $0^\circ \leq \theta_{SB} \leq 90^\circ$

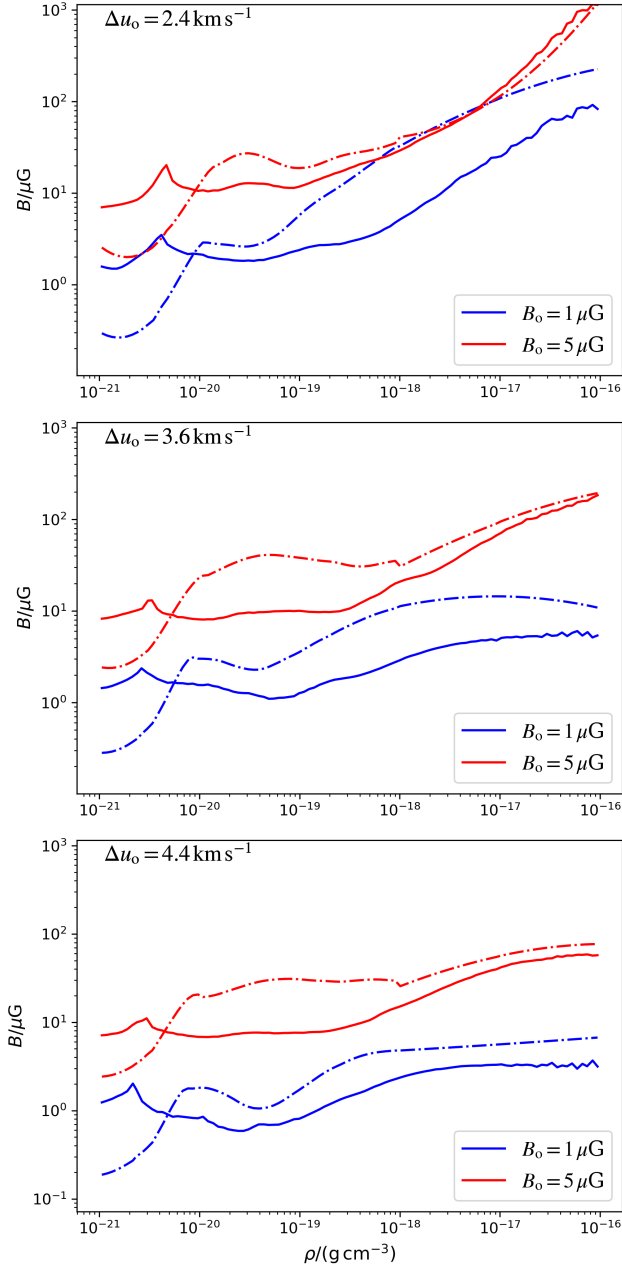


Figure 6. The mean magnetic field as a function of density, at $t_{10\%}$, for collisions at different velocities: *Top Panel*, $\Delta u_0 = 2.4 \text{ km s}^{-1}$; *Middle Panel*, $\Delta u_0 = 3.6 \text{ km s}^{-1}$; *Bottom Panel*, $\Delta u_0 = 4.4 \text{ km s}^{-1}$. Results are presented separately for the axial component of the field, B_x (solid lines), and for the lateral component, B_{yz} (dash-dot lines). The blue curves are for $B_0 = 1 \mu\text{G}$, and the red curves are for $B = 5 \mu\text{G}$. Density runs from the initial density of the clouds ($10^{-21} \text{ g cm}^{-3}$) to the density for star-system creation ($10^{-16} \text{ g cm}^{-3}$).

For slower collisions, the *Layer Accumulation* and *Layer Fragmentation* phases are slower, and there is significant *Lateral Contraction*, so the field is amplified significantly by compression. For example, with $B_0 = 5 \mu\text{G}$ and $\Delta u_0 = 2.4 \text{ km s}^{-1}$, the field is amplified by a factor ~ 200 over the 10^5 -fold density increase between $10^{-21} \text{ g cm}^{-3}$ and $10^{-16} \text{ g cm}^{-3}$.

Thus the rate of increase of the field with increasing density is limited to $\alpha_{B\rho} \equiv d \ln(B)/d \ln(\rho) \lesssim 1/2$. This exponent is significantly

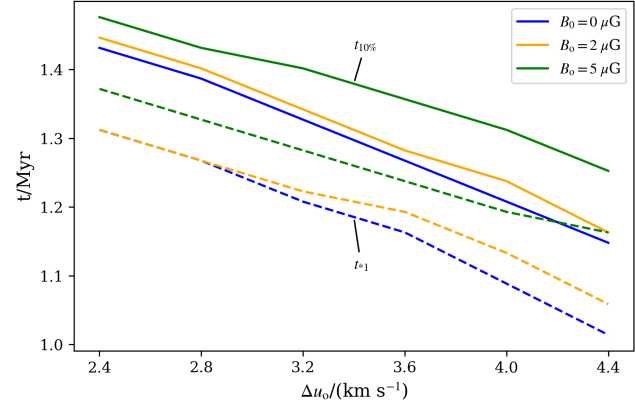


Figure 7. The time at which the first star-system forms, $t_{\star 1}$ (dashed curves), and the time at which 10% of the mass has been converted into star-systems, $t_{10\%}$ (solid curves), as a function of collision velocity, for different initial magnetic field strengths: no field, $B_0 = 0 \mu\text{G}$ (blue); intermediate field, $B_0 = 2 \mu\text{G}$ (orange); and strong field, $B_0 = 5 \mu\text{G}$ (green). For each combination of B_0 and Δu_0 we show the average from three different realisations.

lower than the values for homologous 3D contraction ($\alpha_{B\rho} = 2/3$) or homologous 2D contraction orthogonal to the field ($\alpha_{B\rho} = 1$).

Secondly, the critical field strength required to inhibit star-system formation in a core is $B_{\text{sink}} \simeq 1.6 \text{ mG}$ (see Equation 4.1). If the field approaches this value, star-system formation is delayed while additional mass is accumulated by the core, and star-systems form slightly later, with slightly higher initial masses. However, from Figure 6 we see that the field in material that might be incorporated into a star-system, i.e. material with density close to $\rho \sim 10^{-16} \text{ g cm}^{-3}$, only approaches this critical field strength in the extreme case of strong initial field, $B_0 = 5 \mu\text{G}$, and slow collision velocity, $\Delta u_0 = 2.4 \text{ km s}^{-1}$ (see the red curve on the top panel of Figure 6). Even in this case it doesn't reach B_{sink} .

Thirdly, the field in material that is about to be incorporated into a star-system is always approaching equipartition, $B_{yz} \sim 2^{1/2} B_x$. Furthermore, where the field has not reached equipartition, the lateral component is dominant, $B_{yz} > 2^{1/2} B_x$. This is the field component that is closely aligned with the filaments along which material flows into cores.

The magnetic field in gas that is about to be accreted by a star-system is higher when the collision velocity is low, because there is then a longer *Layer Accumulation* phase, and therefore more time for *Lateral Contraction* to amplify B_x on its own. Consequently the subsequent lateral motions that fragment the layer and establish approximate equipartition between the field components ($B_{yz} \sim 2^{1/2} B_x$) start with a larger seed field.

4.6 Star-system formation timescales

Figure 7 shows, for different values of the initial magnetic field strength, B_0 , how the time at which the first star-system forms, $t_{\star 1}$, and the time at which 10% of the mass has been converted into star-systems, $t_{10\%}$, vary with collision velocity, Δu_0 .

$t_{\star 1}$ decreases with increasing Δu_0 because the *Layer Accumulation* phase is shorter when the clouds collide at higher speed. And $t_{\star 1}$ decreases with decreasing B_0 because the *Layer Fragmentation* phase is shorter when the field is weaker.

The duration of star formation, $\Delta t_{\text{SF}} = t_{10\%} - t_{\star 1} \simeq 0.11 \pm 0.01 \text{ Myr}$,

is approximately independent of both the collision speed and the initial magnetic field strength. There are two reasons for this.

Firstly, by the time star-system creation starts at densities $\rho \gtrsim 10^{-16} \text{ g cm}^{-3}$, memory of the initial supersonic collision velocity has been erased in shocks. The dominant bulk velocities have been generated by gravitational fragmentation and are sub- or trans-sonic.

Secondly, the cores that form star-systems are all magnetically supercritical,

$$B < B_{\text{sink}} = 2\pi G^{1/2} \rho_{\text{sink}} R_{\text{sink}} \sim 1.6 \text{ mG}; \quad (4.1)$$

see Section 4.5 and Figure 6 for typical B values at star-system creation, and Chandrasekhar & Fermi (1953) for the expression for B_{sink} . Once star-forming material has been collected into a core, the timescale for star formation is regulated by the interplay of self-gravity, sub- or trans-sonic turbulence, and thermal pressure. It is therefore approximately independent of B_0 and Δu_0 .

4.7 Masses of star-systems

Figure 8 shows the mass functions obtained with different collision velocities, Δu_0 , for cases with no magnetic field ($B_0 = 0$, top 8 panels), and for cases with a relatively strong magnetic field ($B_0 = 5 \mu\text{G}$, bottom 8 panels). Each mass function represents the combination of three different realisations with the same B_0 and Δu_0 . The value of Δu_0 is indicated in the right margin. The distributions are coloured so as to draw attention to $(B_0, \Delta u_0)$ combinations that deliver similar mass functions, in particular the purple, dark blue, pale blue and cyan mass functions.

With weak (or no) magnetic field and/or relatively high collision velocity, the star formation in the shock compressed layer subscribes to a *Spiders Web* morphology. It delivers a relatively narrow mass function centred on $\sim 1 M_\odot$, and few extreme masses (few very low masses due to dynamical ejection, and few very high masses due to competitive accretion), as shown at the top of Figure 8.

With strong magnetic field and/or relatively low collision velocity, the star formation subscribes to an *Hub Filament* morphology. It again delivers a relatively narrow mass function, but now the mode of the mass function is shifted to lower values and depends on both B_0 and Δu_0 . It shifts to lower values as B_0 is decreased, or Δu_0 is increased, as shown at the bottom of Figure 8. In addition there are always a few extremely massive star-systems formed by competitive accretion in the central hub, and a few very low-mass star-systems formed by dynamical ejection.

Between these limits, there is a progression that can be seen in both the non-magnetic case (top panels of Figure 8) and the strong-field case (bottom panels of Figure 8). This progression represents the transition from *Hub Filament* star formation (at higher B_0 and/or lower Δu_0) to *Spiders Web* star formation (at lower B_0 and/or higher Δu_0).

If we focus on the non-magnetic cases (top panels of Figure 8), the transition from *Hub Filament* to *Spiders Web* takes place around $\Delta u_0 = 3.0 \text{ km s}^{-1}$. Immediately above, at $\Delta u_0 = 3.2 \text{ km s}^{-1}$ (dark blue mass function) there is still a strong peak at $\sim 1 M_\odot$ (similar to the purple one at $\Delta u_0 = 3.6 \text{ km s}^{-1}$), but there is also a growing extension to lower masses. Immediately below, at $\Delta u_0 = 2.8 \text{ km s}^{-1}$ (pale blue mass function) the peak at $\sim 1 M_\odot$ has declined, and the main peak is at $\sim 0.2 M_\odot$. At $\Delta u_0 = 2.4 \text{ km s}^{-1}$ (cyan mass function), the peak at $\sim 1 M_\odot$ has almost completely disappeared, and the mass function is dominated by the peak at $\sim 0.2 M_\odot$.

The same transition can be seen in the cases with strong magnetic field ($5 \mu\text{G}$, bottom panels of Figure 8), but in this case the transition occurs around $\Delta u_0 = 4.2 \text{ km s}^{-1}$ (rather than $\Delta u_0 \sim 3.0 \text{ km s}^{-1}$). This

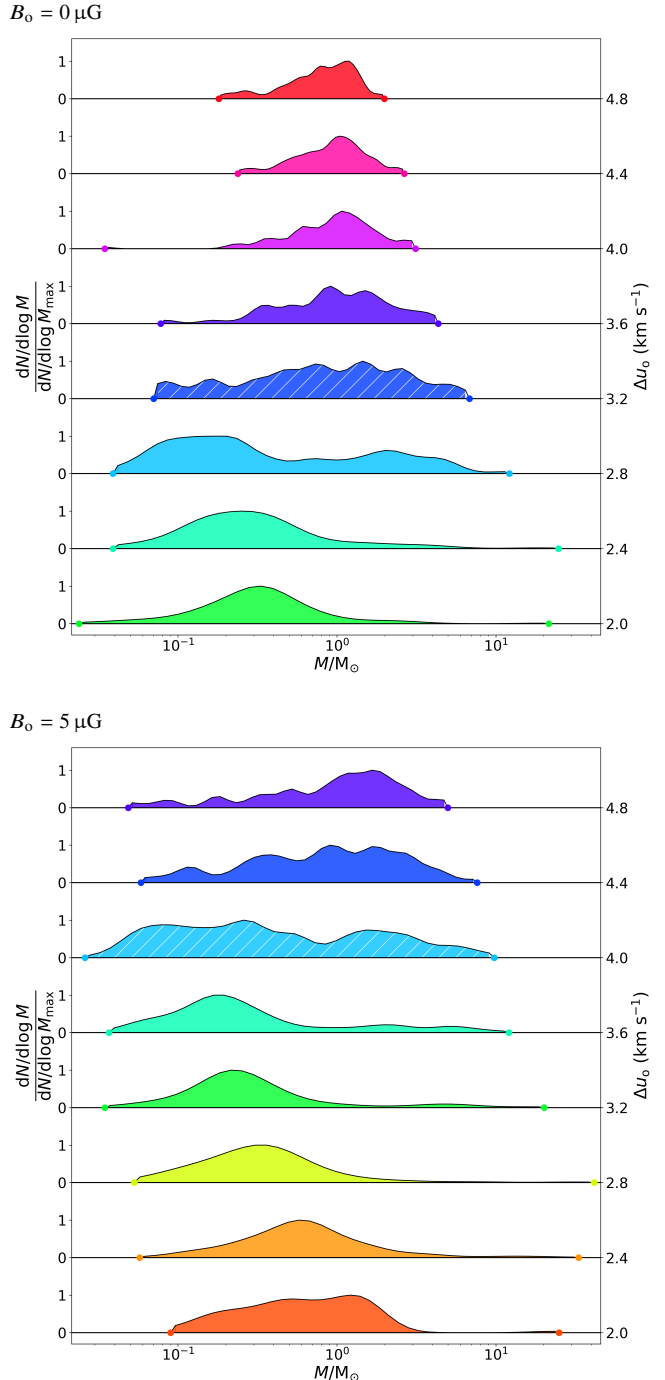


Figure 8. Mass functions for six different collision velocities, Δu_0 , as indicated on the righthand axis and represented by different colours. *Top 8 Panels*: no magnetic field ($B_0 = 0$); *Bottom 8 Panels*: strong magnetic field, $B_0 = 5 \mu\text{G}$. In each case there is a dot marking the minimum and maximum mass; since each combination of B_0 and Δu_0 is only represented by ~ 100 star-systems, these extrema are only indicative. The distributions are normalised so that the peak is unity. The colours are selected to draw attention to the fact that the distributions with and without magnetic field are very similar, if one allows that increased magnetic field is equivalent to reduced collision velocity.

can be seen by comparing the *purple*, *dark blue*, *pale blue* and *cyan* mass distributions on Figure 8. As in the non-magnetic cases the transition marks a switch from the *Hub Filament* morphology at low collision velocity to the *Spiders Web* morphology at high collision velocity.

4.8 The spatial distribution of star-systems

Figure 9 shows a selection of Minimum Spanning Trees (MSTs) for the positions of the star-systems projected onto the $x = 0$ plane. The top six panels are for the non-magnetic case ($B_0 = 0$), and the bottom six panels are for the strong magnetic field case ($B_0 = 5 \mu\text{G}$). Panels in the left column represent relatively slow collisions, with $\Delta u_0 = 2.4 \text{ km s}^{-1}$; panels in the central column represent intermediate-velocity collisions, with $\Delta u_0 = 3.6 \text{ km s}^{-1}$; and panels in the right column represent relatively fast collisions, with $\Delta u_0 = 4.0 \text{ km s}^{-1}$. For each $(B_0, \Delta u_0)$ combination there is an upper panel showing the MST of the initial (i.e. formation) positions, and a lower panel showing the MST of the final ($t_{10\%}$) positions. The initial positions are *de facto* not simultaneous, whereas the final positions are simultaneous.

In an **EXTREME** *Hub Filament* setup, the collision is so slow, and/or the field so strong, that the *Layer Accumulation* and *Layer Fragmentation* phases only get started after there has been considerable *Lateral Contraction*. Because *Lateral Contraction* is non-homologous (i.e. the centre of the shock-compressed layer contracts laterally on a shorter timescale than the outer parts) the filaments are dragged into radial orientations, and the shock compressed gas is fed into the central hub, before many star-systems condense out. Once they do, competitive accretion creates a few very massive star-systems. At the same time there are violent dynamical ejections creating a diaspora of very low-mass star-systems. The $[B_0, \Delta u_0] = [5 \mu\text{G}, 2.4 \text{ km s}^{-1}]$ case, with *orange* MSTs on Figure 9, is an example of an **EXTREME** *Hub Filament* setup. The spatial distribution of star-systems at formation is extremely compact, and the MST at $t_{10\%}$ is very extended due to dynamical ejections.

In a **MODERATE** *Hub Filament* setup, the collision is sufficiently slow, and/or the field sufficiently strong, that the *Layer Accumulation* and *Layer Fragmentation* phases proceed quite slowly, and there is sufficient time for some *Lateral Contraction* before they are complete. The filaments are dragged into radial orientations, so that gas and forming star-systems are funnelled into a central hub. Here they continue to grow by accretion, unless they are ejected dynamically. The $[B_0, \Delta u_0] = [0 \mu\text{G}, 2.4 \text{ km s}^{-1}]$ and $[5 \mu\text{G}, 3.2 \text{ km s}^{-1}]$ cases, with *green* MSTs on Figure 9, are examples of **MODERATE** *Hub Filament* setups. The MST at $t_{10\%}$ is more extended than the MST at formation, by virtue of the dispersed positions of the dynamically ejected star-systems, but the difference is not as marked as for the (*orange*) **EXTREME** *Hub Filament* setup.

In a **MODERATE** *Spiders Web* setup, the collision is sufficiently fast, and/or the field sufficiently weak, that the *Layer Accumulation* and *Layer Fragmentation* phases proceed quite rapidly. There is enough time for a little *Lateral Contraction*, but not enough for the filaments to be dragged into radial orientations. Consequently there is a *Spiders Web* of intersecting filaments, which spawn an array of star-systems. The lateral extent of the array is reduced somewhat by *Lateral Contraction*. The $[B_0, \Delta u_0] = [0 \mu\text{G}, 3.2 \text{ km s}^{-1}]$ and $[5 \mu\text{G}, 4.0 \text{ km s}^{-1}]$ cases, with *blue* MSTs on Figure 9, are examples of **MODERATE** *Spiders Web* setups. The spatial distribution of star-systems at formation and at $t_{10\%}$ are similar, because there are not many dynamical ejections.

In an **EXTREME** *Spiders Web* setup, the collision is so fast, and the field is so weak, that the *Layer Accumulation* and *Layer Fragmentation*

phases are completed before there is enough time for significant *Lateral Contraction*, and therefore before there is time to decrease the lateral extent of the shock-compressed layer, or to drag the filaments into radial orientations. Consequently *Layer Fragmentation* produces an extended *Spiders Web* of intersecting filaments, which in turn spawn a widely dispersed array of star-systems. The $[B_0, \Delta u_0] = [5 \mu\text{G}, 4.0 \text{ km s}^{-1}]$ case, with *purple* MSTs on Figure 9, is an example of an **EXTREME** *Spiders Web* setup. The spatial distributions of star-systems at formation and at $t_{10\%}$ are similar.

Thus there is always a progression from **(a)** an extreme *Hub Filament* morphology producing a monolithic cluster with the formation of star-systems confined to a very compact initial MST, but then high ejection speeds producing an extended final MST at $t_{10\%}$ (*orange plots*); through **(b)** (ii) a less extreme *Hub Filament* morphology with the formation of star-systems in a moderately compact initial MST and a few ejections extending the final MST with a few straggly arms at $t_{10\%}$ (*green plots*); on to **(c)** a relatively compact *Spiders Web* morphology with a moderately extended initial MST that has not expanded much by $t_{10\%}$ (the final MST), because there have not been many dynamical ejections (*blue plots*); and finally on to **(d)** a broad *Spiders Web* morphology producing an array of isolated star-systems, where again the MST does not change much between formation (initial MST) and $t_{10\%}$ (final MST), because there are few energetic dynamical ejections (*purple plots*).

The spatial distribution of the star-systems can be characterised by two parameters. The first is the normalised mean MST edge-length,

$$\bar{m} = \frac{N-1}{(AN)^{1/2}} \sum_{n=1}^{n=N-1} \{m_n\}. \quad (4.2)$$

Here N is the number of star-systems, A is the area of the convex hull enclosing their projected positions (A is computed using `scipy.spatial.ConvexHull`), and m_n is the length of the n^{th} edge on the MST. There are $N-1$ edges on the MST.

The second is the normalised mean correlation length,

$$\bar{s} = \left(\frac{\pi}{A}\right)^{1/2} \frac{2}{N(N-1)} \sum_{i=1}^{i=N-1} \sum_{j=i+1}^{j=N} \{s_{ij}\}. \quad (4.3)$$

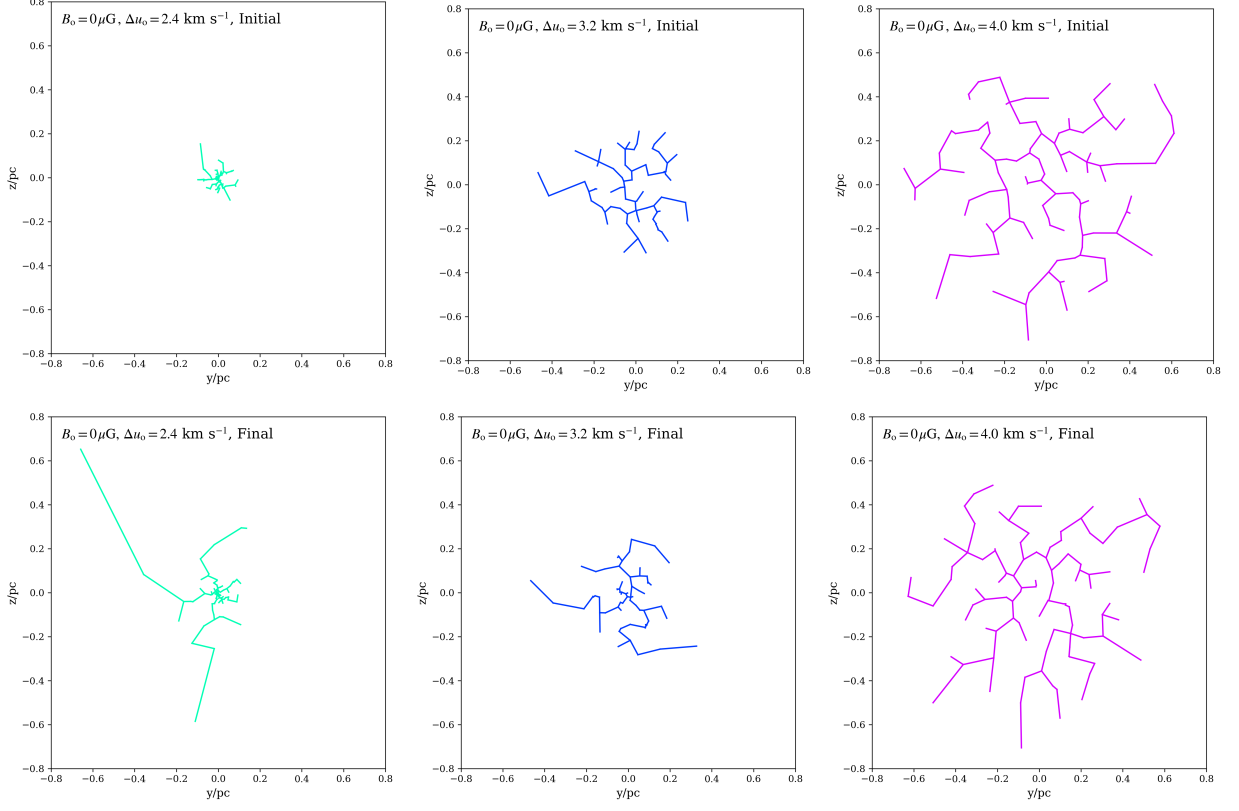
Here s_{ij} is the projected separation between star-systems i and j , and the sum is now over all pairs of star-systems. Thus there are $N(N-1)/2$ correlation lengths.

We note that the normalisations in Equations 4.2 and 4.3 means that the values of \bar{m} and \bar{s} do not reflect the physical size of the star-system distribution, but just the sizes of star-system separations relative to the overall size of the distribution, and the number of separations considered.²

Figure 10 shows the combinations of \bar{m} and \bar{s} for the MSTs of the initial and the final star-system locations. The $[\bar{m}, \bar{s}]$ combinations fall into two groupings, a *lower grouping* at $\bar{m} \lesssim 0.5$ and $\bar{s} \lesssim 0.5$, representing *Hub Filament* morphologies; and an *upper grouping* at $\bar{m} \gtrsim 0.5$ and $\bar{s} \gtrsim 0.7$, representing *Spiders Web* morphologies. In almost all cases the shift from the formation $[\bar{m}, \bar{s}]$ combination to the corresponding final $[\bar{m}, \bar{s}]$ combination is towards lower \bar{m} and lower

² The values of \bar{m} and \bar{s} can be combined to compute $Q = \bar{m}/\bar{s}$ (Cartwright & Whitworth 2004). Q can then be used (a) to distinguish fractal star clusters with no central concentration, from spherical star clusters with a smooth radial density gradient, and hence (b) to obtain either a measure of the fractal dimension, \mathcal{D} , or the radial density exponent, $-d\ln(n_\star)/d\ln(R)$. However this interpretation is not pertinent here. The clusters are neither smooth, nor spherical, nor fractal (in the sense of having an approximately self-similar nested hierarchy of structures).

$B_0 = 0 \mu\text{G}$



$B_0 = 5 \mu\text{G}$

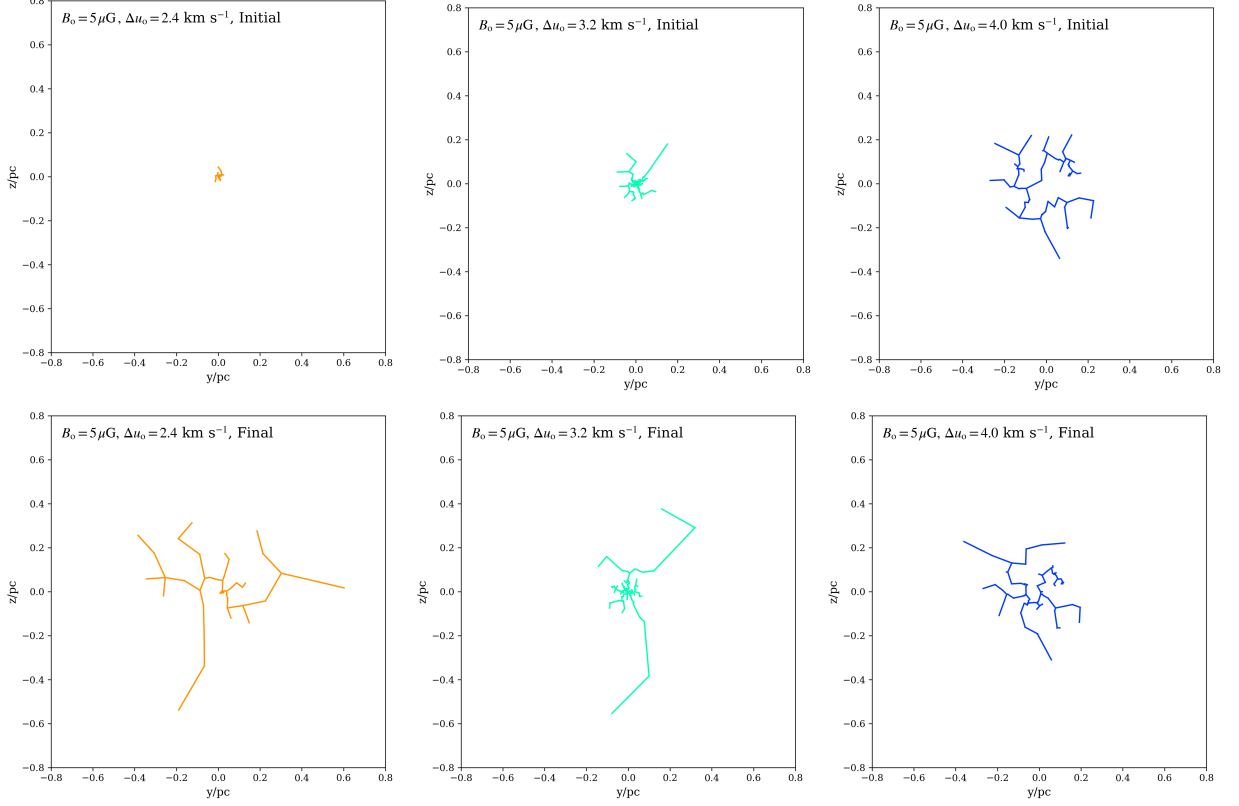


Figure 9. Minimum spanning trees (MSTs) for star-system positions projected onto the $x=0$ plane. *First & Second Rows:* initial and final star-system positions with no magnetic field ($B_0 = 0$). *Third & Fourth Rows:* initial and final star-system positions with strong magnetic field, $B_0 = 5 \mu\text{G}$. *Left Column:* $\Delta u_0 = 2.4 \text{ km s}^{-1}$; *Middle Column:* $\Delta u_0 = 3.6 \text{ km s}^{-1}$; *Right Column:* $\Delta u_0 = 4.0 \text{ km s}^{-1}$. The MSTs are coloured to draw attention to $(B_0, \Delta u_0)$ combinations that have similar initial star-system MSTs and similar final star-system MSTs.

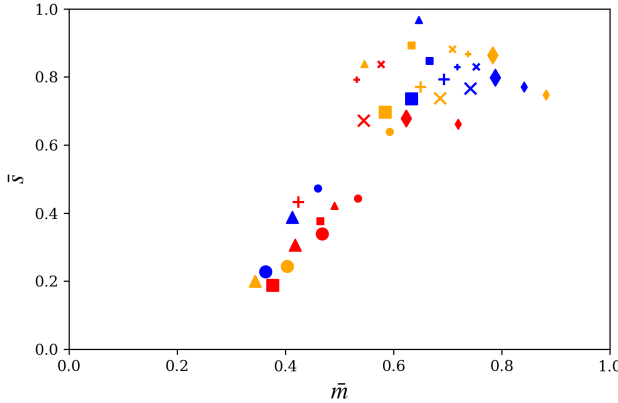


Figure 10. The locations of star-system formation-site and final-position MSTs, on the (\bar{m}, \bar{s}) plane. Magnetic field strengths are colour-coded: $B_0 = 0 \mu\text{G}$ (blue), $B_0 = 2 \mu\text{G}$ (yellow), and $B_0 = 5 \mu\text{G}$ (red). Filled circles, triangles, squares, pluses, crosses and diamonds correspond to collision velocities $\Delta u_0 = 2.4, 2.8, 3.2, 3.6, 4.0$ and 4.4 km s^{-1} , respectively. Smaller symbols indicate MSTs based on formation positions. Larger symbols indicate MSTs based on final positions at $t_{10\%}$.

\bar{s} , as individual star-systems tend to migrate closer to their nearest neighbours as time advances.

For clear *Hub Filament* morphologies (strong B_0 and/or small Δu_0) the formation and final $[\bar{m}, \bar{s}]$ combinations are both in the *lower grouping* because most – but not all – star-systems are formed in close proximity to one another in the central hub. A few are formed in the filaments feeding the central hub, and therefore the convex hull has an area much larger than the hub.

For clear *Spiders Web* morphologies (weak/no B_0 and/or large Δu_0) the formation and final $[\bar{m}, \bar{s}]$ combinations are both in the *upper grouping* because most – but not all – star-systems are formed in isolation, from a single core. The numerical experiments do not have enough resolution to capture the formation of a small subcluster from each core, although this is what we would expect to happen in nature (see e.g. Ambrose & Whitworth 2024, 2025).

For transitional setups in the strip of $(B_0, \Delta u_0)$ parameter space intermediate between clear *Hub Filament* morphologies and clear *Spiders Web* morphologies, the formation $[\bar{m}, \bar{s}]$ combinations are in the *upper grouping* mimicking the dispersed formation sites of a *Spiders Web* morphology, and the final $[\bar{m}, \bar{s}]$ combinations are in the *lower grouping* mimicking the centrally concentrated final sites of an *Hub Filament* morphology.

5 DISCUSSION

5.1 Overview

The numerical experiments presented here pertain to artificially simplified setups. This approach has been adopted so that the parameter space defining the initial conditions is small, and therefore it is more straightforward to identify cause and effect. In this case there are just two parameters, the initial magnetic field, B_0 , and the collision velocity, Δu_0 .

Equivalently we could use the dimensionless parameters β_0 and \mathcal{M}_0 . Here, $\beta_0 = B_0/B_{\text{crit}}$ (where $B_{\text{crit}} = 2\pi G^{1/2} \rho_0 R_0$ is the field strength required for magnetic support to balance the self-gravity of the cloud, on global scales), and $\mathcal{M}_0 = u_0/a_0$ is the Mach Number of the cloud velocities.

It turns out that this is in effect a one-parameter family, with an increase in the initial magnetic field equivalent to a reduction in the collision velocity. The single parameter is $\Delta u_0 \{1 - (B_0/B_{\text{crit}})^2\}$ or $\mathcal{M}_0 \{1 - \beta_0^2\}$.

5.2 Limitations of the model

In this section we consider the additional physical effects that would be most likely to change the results, and how they might change them.

5.2.1 'Turbulent' clouds

Real clouds have internal structure, manifest as both systematic and random variations in magnetic field, radiation field, density, temperature, chemical composition, and bulk velocity. Including these variations will disrupt the regularity and coherence of the shock-compressed layer.

For setups with low/no initial magnetic field and/or high collision velocity, there should still be widely distributed cores, as in the *Spiders Web* morphology, but there will be a dispersion in the times at which these cores start forming stars, and therefore also a dispersion in the times at which they finish forming stars.

For setups with high initial magnetic field and/or low collision velocity, as in the *Hub Filament* morphology, there will be a dispersion in the times at which filaments form, and hence some variance in their coherence as they merge and are dragged into radial orientations. This is likely to reduce the number of dominant large-scale radial filaments, producing more realistic *Hub Filament* morphologies.

5.2.2 Collisions at finite impact parameter

Real clouds will not collide head-on (i.e. with their centres of mass aligned with the collision velocity). Collisions at finite impact parameter will deliver systematic angular momentum, \mathbf{L}_0 , to the shock-compressed layer, and the resulting shear will inhibit contraction orthogonal to \mathbf{L}_0 .

As a result, the dominant filaments should be preferentially aligned orthogonal to \mathbf{L}_0 . The filaments in observed *Hub Filament* morphologies often show a preferential orientation, rather than being statistically isotropic as in the head-on CCCs considered here.

5.2.3 Alignment of the magnetic field

There should be fundamental differences in the phenomenology of CCCs if the magnetic field is not aligned with the collision velocity.

In the extreme case where the field is orthogonal to the collision velocity, the gas will only be significantly compressed if the initial field is much smaller, $B_0 \ll 5 \mu\text{G}$, and/or the collision velocity is much higher, $\Delta u_0 \gg 5 \text{ km s}^{-1}$, than the values treated in the setups considered here.

If the field is at an intermediate angle, θ_{uB} , to the collision velocity (intermediate between 0° and 90°), the constraints on B_0 and Δu_0 for significant compression are relaxed (relative to the orthogonal case), but they are still quite restrictive for all but the smallest θ_{uB} .

It seems likely that the velocities of clouds involved in CCCs that initiate star formation are preferentially aligned with the local magnetic field.

5.2.4 Mass resolution

There should be fundamental differences in the mass function of star-systems if the resolution were improved, and this needs to be explored. In particular, a core formed in the shock compressed layer would be expected to spawn a small subcluster, and the subcluster would likely include some stars that are too small to have been resolved here.

Since (a) each SPH particle has mass $m_{\text{SPH}} = 0.001 M_{\odot}$ and ~ 57 neighbours, these experiments cannot resolve star-systems below the Hydrogen Burning Limit at $\sim 0.075 M_{\odot}$ (i.e. Brown Dwarfs and Planetary Mass Objects), and therefore the mass functions are truncated artificially below this mass.

However, it is also the case that, in the Milky Way near the Sun, stars below the Hydrogen Burning Limit contribute very little to the overall mass budget (less than 2%), so the mass functions obtained here may be an acceptable approximation to star-system mass functions.

5.2.5 Other limitations, and termination of the experiments

We would not expect fundamental differences in the large-scale spatial distribution of stars, since this is determined by (a) the shape of the filamentary network, and (b) where that network delivers gas that is dense enough to condense out as stars.

We would not expect fundamental differences in the large-scale phenomenology of star formation if two colliding clouds with different masses and/or radii were invoked, provided the clouds had comparable surface-densities. If they had very different surface-densities, the phenomenology of the collision might be very different.

We would not expect fundamental differences in the large-scale phenomenology of star formation initiated by CCCs if the thermodynamics, chemistry and radiation transport were treated in more detail, or the assumption of ideal MHD were relaxed — but we would expect significant differences if the experiments were pursued to higher densities.

In particular, feedback would become important. This would be especially important in the monolithic star clusters that form more massive stars (Georgatos & Whitworth, in prep.). It would also be important in the evolution on scales below our resolution limit ($\sim 10^3$ AU), where small subclusters and binary/multiple systems are formed.

In real clouds star formation is self-limiting, and appears to terminate once 5 to 20% of the available mass has been converted into stars. The artificial device of terminating the experiments once 10% of the mass has been converted into star-systems is therefore a serious limitation as regards the efficiency of star formation and the mass function below The Hydrogen Burning Limit, but treating feedback lies outside the scope of this paper.

Since star formation is a chaotic process, we have performed three realisations for each $(B_0, \Delta u_0)$ combination, and collated the results to obtain the statistics presented in Figures 3, 5, 7, 8, 10 and 6. Whilst it would be better to have a larger number of realisations, the systematic trends with increasing $\Delta u_0 \{1 - (B_0/B_{\text{crit}})^2\}$ that constitute the main conclusions of this paper appear to be robust, i.e. more pronounced than stochastic variance.

6 CONCLUSIONS

We have investigated the role of magnetic fields in head-on cloud/cloud collisions between spherical clouds with mass $500 M_{\odot}$ and radius 2 pc. The clouds have uniform density and the magnetic field is aligned

with the collision velocity. Therefore different setups are characterised by the initial field strength, B_0 , and the collision velocity, Δu_0 .

- Although we have considered setups defined by two independent parameters, B_0 and Δu_0 , most of the results appear to subscribe to a one-dimensional family. An increase in the magnetic field is equivalent to a decrease in the collision velocity, in that both have the effect of slowing down the process of *Layer Accumulation*, and thereby creating more time for *Lateral Contraction* of the shock compressed layer. This in turn shifts the pattern of star formation from the *Spiders Web* morphology to the *Hub Filament* morphology, hence away from dispersed star formation in small relatively isolated cores with a relatively narrow mass function, and towards star formation in a monolithic centrally concentrated star cluster with a broader mass function.

- The switch from the *Spiders Web* morphology for faster ‘magnetic-weak’ setups, to the *Hub Filament* morphology for slower ‘magnetic-strong’ setups, occurs at collision velocity

$$\Delta u_0 \sim 3 \text{ km s}^{-1} \{1 - (B_0/10\mu\text{G})^2\}^{-1}. \quad (6.1)$$

- For slower and/or ‘magnetic-strong’ setups, $\Delta u_0 \lesssim 2.8 \text{ km s}^{-1} \{1 - (B_0/10\mu\text{G})^2\}^{-1}$, the shock-compressed layer fragments into an *Hub Filament* morphology of radially oriented filaments that feed material into a central hub, and a few star-systems condense out of the filaments and fall into the hub alongside the gas. Once in the hub more star-systems condense out and compete to accrete the remaining gas. The filaments tend to be somewhat broader, $0.04 \text{ pc} \lesssim \text{FWHM} \lesssim 0.17 \text{ pc}$. A small number of star-systems grow to high mass by virtue of being able to compete for additional mass from the large reservoir in the central monolithic hub.

- For faster and/or ‘magnetic-weak’ setups, $\Delta u_0 \gtrsim 3.2 \text{ km s}^{-1} \{1 - (B_0/10\mu\text{G})^2\}^{-1}$, the shock-compressed layer fragments into a *Spiders Web* morphology of filaments, relatively small and isolated prestellar cores condense out, often at the intersections of the filaments, and these cores then spawn a dispersed array of star-systems. The filaments tend to be quite narrow, $0.02 \text{ pc} \lesssim \text{FWHM} \lesssim 0.10 \text{ pc}$. High-mass star-systems, and therefore presumably high-mass stars ($\gtrsim 10 M_{\odot}$) are rare, because the individual cores have small mass reservoirs.

- There are also transitional setups for intermediate values of $\Delta u_0 \sim 3 \text{ km s}^{-1} \{1 - (B_0/10\mu\text{G})^2\}^{-1}$, and a clear monotonic sequence in the statistical descriptors of star formation — filament widths, star-system mass functions, initial and final spatial distributions of star-systems, degrees of magnetic field amplification — with increasing $\Delta u_0 \{1 - (B_0/10\mu\text{G})^2\}$.

- The magnetic field in a filament tends to be aligned with the spine of the filament, but there are also places where the field is approximately perpendicular to the spine and the field reverses direction across the filament.

- Once star formation starts, the rate of star formation is essentially independent of the initial setup, and of order $10^3 M_{\odot} \text{ Myr}^{-1}$.

ACKNOWLEDGMENTS

TG gratefully acknowledges the receipt of an STFC PhD studentship. The numerical experiments were all performed on the Cardiff University Advanced Research Computing facility (ARCCA).

DATA AVAILABILITY

The data are available upon request to TG.

REFERENCES

Ambrose H. E., Whitworth A. P., 2024, *MNRAS*, **535**, 3700

Ambrose H. E., Whitworth A. P., 2025, *MNRAS*, **541**, 3728

André P., et al., 2016, *Astronomy & Astrophysics*, 592, A54

Arzoumanian D., et al., 2011, *Astronomy & Astrophysics*, 529, L6

Balfour S., Whitworth A., Hubber D., Jaffa S., 2015, *Monthly Notices of the Royal Astronomical Society*, 453, 2471

Balfour S., Whitworth A., Hubber D., 2016, *Monthly Notices of the Royal Astronomical Society*, 465, 3483

Bate M. R., Bonnell I. A., Price N. M., 1995, *Monthly Notices of the Royal Astronomical Society*, 277, 362

Cartwright A., Whitworth A. P., 2004, *Monthly Notices of the Royal Astronomical Society*, 348, 589

Chandrasekhar S., Fermi E., 1953, *Astrophysical Journal*, pp 116–141

Dinnbier F., Wünsch R., Whitworth A. P., Palouš J., 2017, *MNRAS*, **466**, 4423

Dobbs C., Pringle J., Duarte-Cabral A., 2015, *Monthly Notices of the Royal Astronomical Society*, 446, 3608

Fukui Y., et al., 2018a, *Publications of the Astronomical Society of Japan*, **70**, S44

Fukui Y., et al., 2018b, *Publications of the Astronomical Society of Japan*, **70**, S46

Fukui Y., Habe A., Inoue T., Enokiya R., Tachihara K., 2021a, *Publications of the Astronomical Society of Japan*, **73**, S1

Fukui Y., Inoue T., Hayakawa T., Torii K., 2021b, *Publications of the Astronomical Society of Japan*, **73**, S405

Gong Y., et al., 2019, *Astronomy & Astrophysics*, 632, A115

Hacar A., Tafalla M., Forbrich J., Alves J., Meingast S., Grossschedl J., Teixeira P. S., 2018, *Astronomy & Astrophysics*, 610, A77

Haworth T., et al., 2015, *Monthly Notices of the Royal Astronomical Society*, **450**, 10

Horie S., Okamoto T., Habe A., 2024, *Monthly Notices of the Royal Astronomical Society*, **527**, 10077

Howard A. D. P., Whitworth A. P., Marsh K. A., Clarke S. D., Griffin M. J., Smith M. W. L., Lomax O. D., 2019, *MNRAS*, **489**, 962

Hsu C.-J., Tan J. C., Christie D., Cheng Y., O'Neill T. J., 2023, *Monthly Notices of the Royal Astronomical Society*, **522**, 700

Inoue T., Fukui Y., 2013, *The Astrophysical Journal Letters*, **774**, L31

Inutsuka S.-I., Miyama S. M., 1992, *ApJ*, **388**, 392

Kitsionas S., Whitworth A. P., 2007, *MNRAS*, **378**, 507

Koch E., Rosolowsky E., 2015, *Monthly Notices of the Royal Astronomical Society*, **452**, 3435

Larson R. B., 1981, *MNRAS*, **194**, 809

Maity A., et al., 2024, *The Astrophysical Journal*, **974**, 229

Morris J. P., Monaghan J. J., 1997, *Journal of Computational Physics*, **136**, 41

Palmeirim P., André P., Kirk J. M., et al. 2013, *Astronomy & Astrophysics*, **550**, A38

Panopoulou G. V., Psaradaki I., Skalidis R., Tassis K., Andrews J. J., 2017, *Monthly Notices of the Royal Astronomical Society*, **466**, 2529

Panopoulou G., Clark S., Hacar A., Heitsch F., Kainulainen J., Ntormousi E., Seifried D., Smith R., 2022, *Astronomy & Astrophysics*, **657**, L13

Price D. J., 2007, *Publications of the Astronomical Society of Australia*, **24**, 159

Price D. J., et al., 2018, *Publications of the Astronomical Society of Australia*, **35**, e031

Priestley F., Whitworth A., 2021, *Monthly Notices of the Royal Astronomical Society*, **506**, 775

Sakre N., Habe A., Pettitt A. R., Okamoto T., 2021, *Publications of the Astronomical Society of Japan*, **73**, S385

Sakre N., Habe A., Pettitt A. R., Okamoto T., Enokiya R., Fukui Y., Hosokawa T., 2022, *Publications of the Astronomical Society of Japan*, **73**, S385–S404

Sakre N., Habe A., Pettitt A. R., Okamoto T., Enokiya R., Fukui Y., Hosokawa T., 2023, *Monthly Notices of the Royal Astronomical Society*, **522**, 4972

Smith R. J., Glover S. C. O., Klessen R. S., Fuller G. A., 2016, *Monthly Notices of the Royal Astronomical Society*, **455**, 3640

Weis M., Walch S., Seifried D., Ganguly S., 2024, *Monthly Notices of the Royal Astronomical Society*, **532**, 1262

Whitworth A. P., 2016, *MNRAS*, **458**, 1815

Whitworth A. P., Bhattacharjee A. S., Chapman S. J., Disney M. J., Turner J. A., 1994a, *MNRAS*, **268**, 291

Whitworth A. P., Bhattacharjee A. S., Chapman S. J., Disney M. J., Turner J. A., 1994b, *A&A*, **290**, 421

Whitworth A., Lomax O., Balfour S., Mège P., Zavagno A., Deharveng L., 2018, *PASJ*, **70**, S55

Whitworth A. P., Priestley F. D., Geen S. T., 2022, *MNRAS*, **517**, 4940

Wu B., Tan J. C., Nakamura F., Van Loo S., Christie D., Collins D., 2017, *The Astrophysical Journal*, **835**, 137

This paper has been typeset from a *TeX/LaTeX* file prepared by the author.